Grain boundary energy function for α iron

Rajchawit Sarochawikasit [a], Cong Wang [b], Poom Kumam [c], Hossein Beladi [d], Taira Okita [e], Gregory S. Rohrer [f,*], Sutatch Ratanaphan [a,c,g,*]

[a] Department of Computer Engineering, King Mongkut's University of Technology Thonburi, 126 Pracha Uthit Rd, Thung Khru, Bangkok 10140, Thailand
[b] Department of Metallurgical Engineering, Northeastern University, Shenyang 110819, China
[c] Center of Excellence in Theoretical and Computational Science Center (TaCS-CoE), King Mongkut's University of Technology Thonburi, 126 Pracha Uthit Rd, Thung Khru, Bangkok 10140, Thailand
[d] Institute for Frontier Materials, Deakin University, Geelong, VIC 3216, Australia
[e] Research into Artifacts, Center for Engineering, School of Engineering, the University of Tokyo, Tokyo, Japan
[f] Department of Materials Science and Engineering, Carnegie Mellon University, Pittsburgh, PA 15213-3890 United States
[g] Department of Tool and Materials Engineering, King Mongkut's University of Technology Thonburi, 126 Pracha Uthit Rd, Thung Khru, Bangkok 10140, Thailand

ARTICLE INFO

ABSTRACT

Polycrystalline α iron has been used in various applications, yet its microstructure design via grain boundary engineering (GBE) is not well established. One limiting factor is that while there are many different grain boundaries in the five-dimensional space of grain boundary types, relatively few of the energies have been determined. In this study, a piece-wise continuous grain boundary energy function for α iron is constructed to fill the entire five-dimensional space of grain boundary types using scaffolding subsets with lower dimensionality. Because the energies interpolated from the grain boundary energy function are consistent with the 408 boundaries that have been calculated using atomistic simulations, the energy function is then employed to generate a larger set of grain boundary energies. Comparisons between the interpolated energies and the measured grain boundary population indicate that they are inversely correlated for the high-energy anisotropy misorientations (those for which the difference between the maximum and minimum grain boundary energies is greater than 0.4 J/m^2). The results suggest that GBE in the α iron should consider the high-energy anisotropy misorientations, rather than the twinning-related grain boundaries (Σ3, Σ9, Σ27a, and Σ27b) as in the case of fcc metals.

1. Introduction

In a wide range of solid materials, microstructure engineering is used to enhance the properties of polycrystals [1–3]. The grain boundary character distribution (GBCD), which is the relative areas of different grain boundary types, influences certain macroscopic properties including, corrosion resistance, mechanical strength, and electrical conductivity [3–9]. Therefore, an important goal in microstructure engineering is to have a sufficient understanding of the microstructural evolution to optimize the GBCD for particular properties [2,3,10]. Many efforts have been made to tailor the properties of polycrystalline body-centered cubic (bcc, α) iron by grain boundary engineering (GBE) of the GBCDs through thermo-mechanical processes [11–16]. However, our understanding of the grain boundary energy distribution (GBED) in the α iron, which plays a significant role in the microstructural evolution, is incomplete. Considering the size of space defined by the five-macroscopic grain boundary parameters (three for the grain boundary misorientation and two for

the plane inclination) [4,5], it is challenging to specify all of the grain boundary energies.

The Bulatov-Reed-Kumar (BRK) grain boundary energy function for face-centered cubic (fcc) metals [17] is one method to specify the energy of any grain boundary. The BRK function, which was recently developed based on a scaffolding of lower-dimensional subsets of low grain boundary energy in Ni, Al, Au, and Cu [18], has been successfully used to interpolate large sets of grain boundary energies in the pure copper [19] and an austenitic steel alloy [20]. The grain boundary energies interpolated using the BRK energy function were not only strongly correlated to simulated grain boundary energies, but also inversely correlated to the measured grain boundary population at fixed misorientations [19,20]. Therefore, it is possible that the same technique can be used to create a grain boundary energy function for α iron.

The goal of this paper is to present a BRK-type energy function for α-iron. There are two possible sets of data to fit the function. The first is a set of measured grain boundary energies (6×10^3 boundaries for discretization of 10°) for a ferritic steel [14] and the second is a set of 408 grain boundary energies computed by simulation [21]. Because the
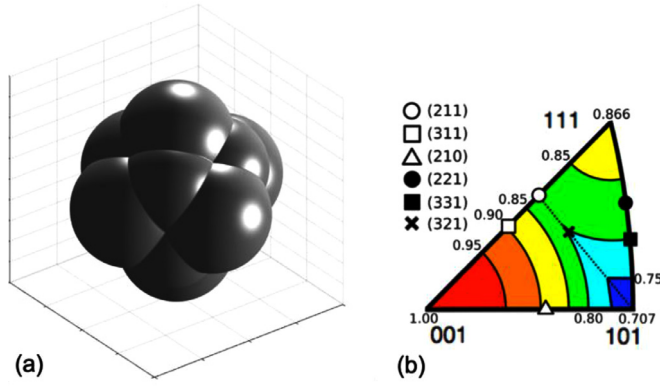

Fig. 1. Density of the first nearest-neighbor bonds (a) and the distribution of surface energy plotted as a function of surface orientation (b). Note that the surface energies are calculated from the nearest-neighbor broken bond model for bcc metals [24] and the units for energy in the figure are scaled with E (100) = 1.00 (energy maximum).

measured grain boundary energies were determined from an iron alloy, and they inherit experimental error from the energy reconstruction method [4,22], we choose the simulated energies as the basis for α iron grain boundary energy function [21]. Even though the calculated grain boundary energy data is more sparse, knowledge of the geometry and topology of the grain boundary energy reduces the number of boundary energy data points that are needed to formulate the grain boundary function [17,23]. To test the validity of the grain boundary energy function, it is compared to measured grain boundary populations, which are expected to be inversely correlated to the grain boundary energy [14]. The remainder of the paper is structured as follows. The concept of grain boundary energy cusps and maxima are described in Section 2. The positions of energy cusps and maxima identified from the simulated data [23] are then used to construct the interpolated functions within scaffoldings sets. The results of grain boundary energy distribution are discussed and compared with the 408 energies determined by simulation in Section 3. In this section, the energies of grain boundaries obtained from the proposed energy function are also compared with the measured grain boundary population [14]. The conclusions are stated in Section 4. The appendix contains supplementary data of grain boundary description and the grain boundary energy function implemented in MATLAB® program AlphaFeGBE, that can be used to compute the energies of arbitrary grain boundaries in the α iron.

2. Methodology

To construct our grain boundary energy function for the α iron, we adopt the procedures and assumptions originally defined by BRK [17]. Specifically, in the multidimensional space of grain boundary energies, cusps (singularities in the energy as a function of the grain boundary parameters) become grooves. By selecting the deepest (lowest energy) grooves from the 408 grain boundaries [21], it is possible to define the grain boundary energy function. Those grooves not included are assumed to be shallow and not significantly different from the interpolated energy. The energy of a grain boundary (ϵ) can be estimated by the total energy to create two surfaces minus the energy gained when the new bonds are formed; $\epsilon = E^1_{(h^1k^1l^1)} + E^2_{(h^2k^2l^2)} - B_{(E^1 \ E^2)}$. For an atomically flat crystal surface, the surface energies are associated with the density of the first nearest-neighbor bonds [24]. While the surface energy can be directly determined from the density of the first nearest-neighbor bonds given by the (hkl) orientation of the surface [24], the surface energy can also be approximated by interpolation between the proximal surfaces with known energies at four grooves crisscrossing as shown in Fig. 1. We hypothesize that the grain boundary energy function for the α iron could be constructed by the subsets of low grain boundary energy (grooves) in the five-macroscopic degrees of freedom with a similar scheme to what have been implemented for the Bulatov-Reed-Kumar (BRK) grain boundary energy function for fcc metals [17]. Particularly, selections of the important energy grooves ($\Sigma 3$, $\Sigma 5$, and $\Sigma 11$) from the 408 grain boundaries [21] are used to define the closed-form grain boundary energy function for the α iron. By assuming that the local minimum energies at the other grooves are rather too shallow or similar to the energies in the proximity of the important grooves, the energy function will be mainly given by the important grooves. To construct the energy function, three subsets of high-symmetry grain boundaries with <100>, <110>, and <111> rotation axes are selected as the scaffolding for the interpolation function for the full five-parameter space. The rotation angle (ξ), the asymmetry tilt angle (η), and the tilt angle (ϕ) are specifically used to classify three subsets; 1-D, 2-D, and 3-D [17]. As shown in Fig. 2, the variation of grain boundary energy in 1D subsets of pure twist ($\xi \neq 0, \eta = 0, \phi = 0$) and symmetric tilt ($\xi \neq 0, \eta = 0, \phi = 1$) boundaries with <100>, <110>, and <111> scaffoldings axes are fitted with the Read-Shockley-Wolf (RSW) function [23,25].

$$f_{rsw}(,_{min},_{max}, a) = \sin\left(\frac{\pi}{2} \frac{\theta - \theta_{min}}{\theta_{max} - \theta_{min}}\right)\left[1 - a\log\sin\left(\frac{\pi}{2}\frac{\theta - \theta_{min}}{\theta_{max} - \theta_{min}}\right)\right] \quad (1)$$

$$\epsilon^{tilt}_{100}(\xi, \eta) = \begin{cases} \epsilon^{stgb}_{100}\left(\frac{\pi}{2} - \xi\right) + f_{rsw}\left(\eta, \frac{\pi}{2}, 0, a^{atgb}_{100}\right)\left[\epsilon^{stgb}_{100}(\xi) - \epsilon^{stgb}_{100}\left(\frac{\pi}{2} - \xi\right)\right], & \epsilon^{stgb}_{100}\left(\frac{\pi}{2} - \xi\right) < \epsilon^{stgb}_{100}(\xi) \\ \epsilon^{stgb}_{100}(\xi) + f_{rsw}\left(\eta, 0, \frac{\pi}{2}, a^{atgb}_{100}\right)\left[\epsilon^{stgb}_{100}\left(\frac{\pi}{2} - \xi\right) - \epsilon^{stgb}_{100}(\xi)\right], & \epsilon^{stgb}_{100}\left(\frac{\pi}{2} - \xi\right) \geq \epsilon^{stgb}_{100}(\xi) \end{cases} \quad (2)$$

$$\epsilon^{tilt}_{110}(\xi, \eta) = \begin{cases} \epsilon^{stgb}_{110}(\pi - \xi) + f_{rsw}\left(\eta, \pi, 0, a^{atgb}_{110}\right)\left[\epsilon^{stgb}_{110}(\xi) - \epsilon^{stgb}_{110}(\pi - \xi)\right], & \epsilon^{stgb}_{110}(\pi - \xi) < \epsilon^{stgb}_{110}(\xi) \\ \epsilon^{stgb}_{110}(\xi) + f_{rsw}\left(\eta, 0, \pi, a^{atgb}_{110}\right)\left[\epsilon^{stgb}_{110}(\pi - \xi) - \epsilon^{stgb}_{110}(\xi)\right], & \epsilon^{stgb}_{110}(\pi - \xi) \geq \epsilon^{stgb}_{110}(\xi) \end{cases} \quad (3)$$

$$\epsilon^{tilt}_{111}(\xi, \eta) = \begin{cases} \epsilon^{stgb,\eta=\pi/3}_{111}(\xi) + f_{rsw}\left(\eta, \frac{\pi}{3}, 0, a^{atgb}_{111}\right)\left[\epsilon^{stgb}_{111}(\xi) - \epsilon^{stgb,\eta=\pi/3}_{111}(\xi)\right], & \epsilon^{stgb,\eta=\pi/3}_{111}(\xi) < \epsilon^{stgb}_{111}(\xi) \\ \epsilon^{stgb}_{111}(\xi) + f_{rsw}\left(\eta, 0, \frac{\pi}{3}, a^{atgb}_{111}\right)\left[\epsilon^{stgb,\eta=\pi/3}_{111}(\xi) - \epsilon^{stgb}_{111}(\xi)\right], & \epsilon^{stgb,\eta=\pi/3}_{111}(\xi) \geq \epsilon^{stgb}_{111}(\xi) \end{cases} \quad (4)$$

For each segment $[_{min},_{max}]$, x varies from 0 and 1. While most of the variations of the grain boundary energy in the 1-D subsets are well characterized by the dimensionless shape parameter (a = 0.5) [17][23],
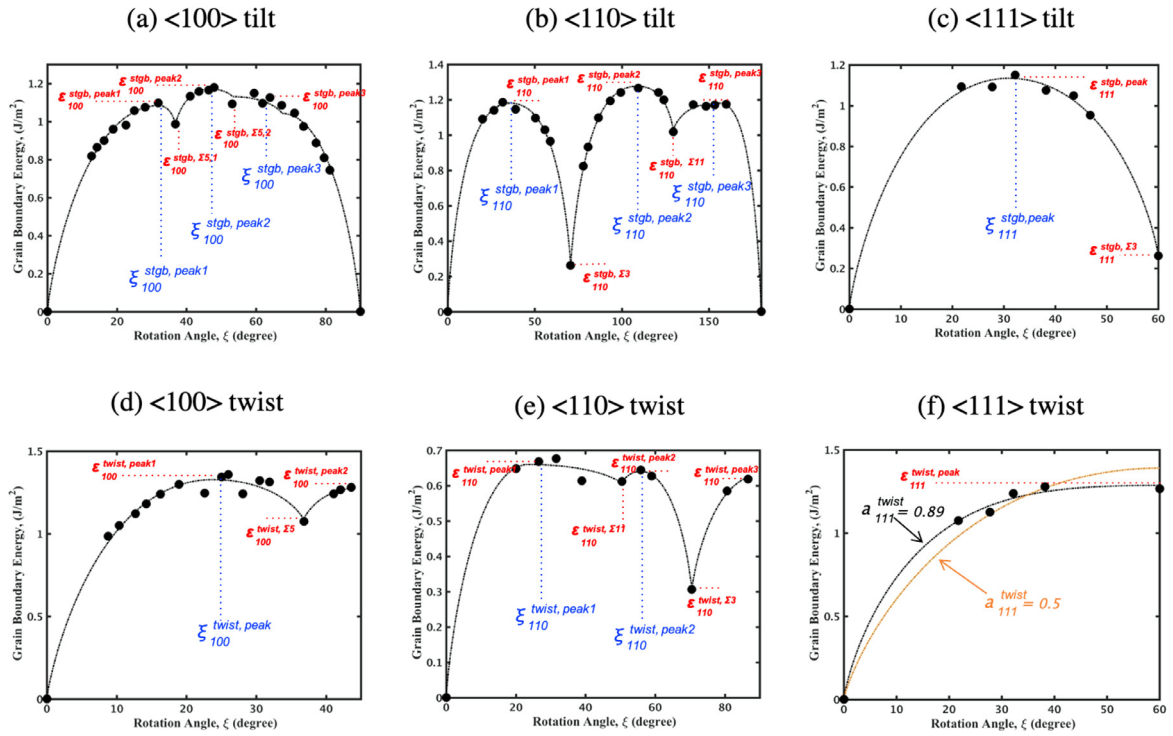
Fig. 2. The energies of 1D subsets of symmetric tilt ($\xi \neq 0, \eta=0, \phi=1$) and pure twist ($\xi \neq 0, \eta=0, \phi=0$) boundaries with <100>, <110>, and <111> scaffoldings axes, that are fitted with the RSW function [25][23]. There are 32 parameters listed in the plots (**Appendix A**).
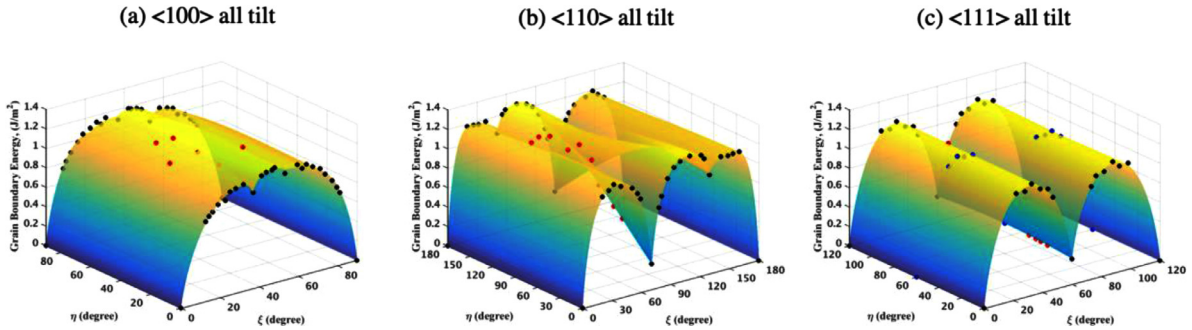

Fig. 3. The energies of 2D subsets of all tilt (symmetric and asymmetric) boundaries, $\epsilon_{hkl}^{tilt}(\xi, \eta)$, with <100>, <110>, and <111> scaffoldings axes. Energies of symmetric tilt ($\xi \neq 0, \eta=0$) boundaries shown in **Fig. 2.** are colored as black circles. Note that the symmetric tilt boundaries, $\epsilon_{111}^{stgb, \eta=\pi/3}(\xi)$, labeled as blue circles in **Fig. 3c**, are classified as 1-D subset. (For interpretation of the references to color in this figure legend, the reader is referred to the web version of this article.)

this parameter does not work well for the (111) twist boundaries in **Fig. 2f**. Therefore, $a_{111}^{twist} = 0.89$ is obtained from the curve fit as listed in **Appendix-A**. For 2D subsets shown in **Fig. 3**, the energies of all tilt (symmetric and asymmetric) boundaries for <100>, <110>, and <111> are linearly interpolated from 1D subsets and the RSW function [23,25] as given by Eq. (2), Eq. (3), and Eq. (4), respectively.

Note that the symmetric tilt boundary with $\eta = \pi/3$, $\epsilon_{111}^{stgb, \eta=\pi/3}(\xi)$, shown in **Fig. 3c** are also fitted with the RSW function [23,25] similar

to what has been done for the <111> symmetric tilt boundaries (see **Fig. 2c**). Based on this approach, three additional fitting parameters, a_{100}^{tilt}, a_{110}^{tilt}, a_{111}^{tilt}, are included (see **Appendix-A**). For 3D subsets, the energies of mixed grain boundaries with <100> and <110> rotation axes are interpolated from 1D, 2D, and the RSW function [23,25] as defined in Eq. (5) and Eq. (6) respectively.

$$\epsilon_{100}^{mix}(\xi, \eta, \phi) = \begin{cases} \epsilon_{100}^{tilt}(\xi, \eta) + f_{rsw}\left(\phi, \frac{\pi}{2}, 0, a_{100}^{mix}\right)\left[\epsilon_{100}^{twist}(\xi) - \epsilon_{100}^{tilt}(\xi, \eta)\right], & \epsilon_{100}^{tilt}(\xi, \eta) < \epsilon_{100}^{twist}(\xi) \\ \epsilon_{100}^{twist}(\xi) + f_{rsw}\left(\phi, 0, \frac{\pi}{2}, a_{100}^{mix}\right)\left[\epsilon_{100}^{tilt}(\xi, \eta) - \epsilon_{100}^{twist}(\xi)\right], & \epsilon_{100}^{tilt}(\xi, \eta) \geq \epsilon_{100}^{twist}(\xi) \end{cases}$$

(5)

$$\epsilon_{110}^{mix}(\xi, \eta, \phi) = \begin{cases} \epsilon_{110}^{tilt}(\xi, \eta) + f_{rsw}\left(\phi, \frac{\pi}{2}, 0, a_{hkl}^{mix}\right)\left[\epsilon_{110}^{twist}(\xi) - \epsilon_{110}^{tilt}(\xi, \eta)\right], & \epsilon_{110}^{tilt}(\xi, \eta) < \epsilon_{110}^{twist}(\xi) \\ \epsilon_{110}^{twist}(\xi) + f_{rsw}\left(\phi, 0, \frac{\pi}{2}, a_{hkl}^{mix}\right)\left[\epsilon_{110}^{tilt}(\xi, \eta) - \epsilon_{110}^{twist}(\xi)\right], & \epsilon_{110}^{tilt}(\xi, \eta) \geq \epsilon_{110}^{twist}(\xi) \end{cases}$$
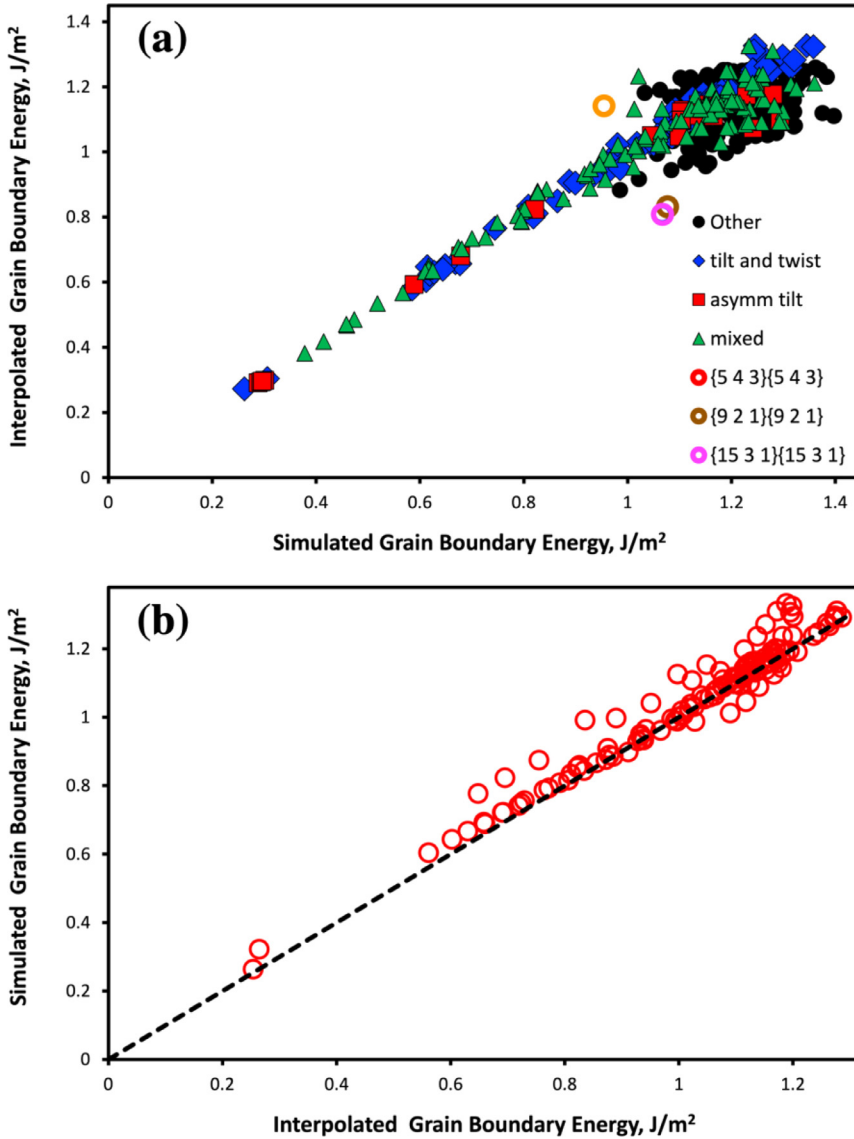
(6)

Fig. 4. The relationship between the simulated energies of grain boundaries in α Fe and the energies of the same boundaries derived from our grain boundary energy function (a). These 408 grain boundaries are assigned into four distinct groups: the 1D subset of pure twist and symmetric tilt boundaries (blue diamonds), the 2D subset of asymmetric tilt boundaries (red squares), the 3D subset of mixed grain boundaries (green triangles), and other types of grain boundaries (black circles). The orange, brown, and purple circles are symmetric boundaries made up from {5 4 3}{5 4 3}, {9 2 1}{9 2 1} and {15 3 1}{15 3 1} planes, respectively. Comparisons of the interpolated and previously simulated grain boundary energies (b). The dash line with a unit slope indicates that the energies interpolated from the grain boundary energy function are strongly correlated with the energies calculated by Tschopp et al. [27]. (For interpretation of the references to color in this figure legend, the reader is referred to the web version of this article.)

This approach is less effective for the energies of mixed grain boundaries with <111>, $\epsilon_{111}^{mix}(\xi, \eta, \phi)$. The values of $\epsilon_{111}^{mix}(\xi, \eta, \phi)$ are better approximated by a parabolic function:

$$\epsilon_{111}^{mix}(\xi, \eta, \phi) = \epsilon_{111}^{twist}(\xi)$$
$$+ \left(\alpha_{111}^{mix} \frac{2\phi}{\pi} - \left(\alpha_{111}^{mix} - 1 \right) \left(\frac{2\alpha_{111}^{mix}}{\pi} \right)^2 \right) \left[\epsilon_{111}^{tilt}(\xi, \eta) - \epsilon_{111}^{twist}(\xi) \right] \quad (7)$$

The fitting parameters for the 3D subset are a_{100}^{mix}, a_{110}^{mix}, and α_{111}^{mix}, $\epsilon_{110}^{mix,\Sigma11}$ and $\epsilon_{110}^{mix,peak}$ (see **Appendix-A**). The energies of arbitrary grain boundaries (ϵ) are approximated using a weighted average over the three scaffolding subsets (1D, 2D, and 3D):

$$\epsilon = \left[\frac{1 + \sum^{W_{hkl}}(d)\, \epsilon_{hkl}(\xi, \eta, \phi)}{1 + \sum^{W_{hkl}}(d)} \right] \epsilon_{RGB} \quad (8)$$

Where ϵ_{RGB} is a high energy of hypothetical random boundary and $w_{hkl}(d)$ is the weighting function given by:

$$W_{hkl}(d) = \left(\frac{1}{f_{rsw}(d, 0, d_{hkl}^{max}, 0.5)} - 1 \right) W_{hkl}^0 \quad (9)$$

Where hkl is one the three primary rotation axes: <100>, <110>, and <111>. To select only the energy that is only proximal to the arbitrary

boundary, the weighting function considers only the boundary with the crystallographic distance $d < d_{hkl}^{max}$ [17]. The fitting parameters for the full interpolation in the 5D are d_{100}^{max}, d_{110}^{max}, d_{111}^{max}, W_{100}^0, W_{110}^0, and W_{111}^0 (see **Appendix-A**).

3. Results and discussion

The closed-form grain boundary energy function for α Fe contains 50 parameters listed in **Table A1**. The simulated and interpolated grain boundaries are compared in **Fig. 4a**. While there are some differences between the energies from simulation and the fitted function for the highest energy boundaries, there is a clear and strong correlation with a correlation coefficient of 0.93. Specifically, energies of the pure twist, symmetric tilt, and tilt boundaries with <100>, <110>, and <111> axes are perfectly described by the RSW function [23,25] (also see **Fig. 2** and **Fig. 3**). The interpolated energies of the {5 4 3}{5 4 3}, {9 2 1}{9 2 1} and {15 3 1}{15 3 1} boundaries differ from the simulated energies by the most significant fraction ($\sim$ 20 %), suggesting that the shape of the scaffolding subsets or the weighting scheme used in **Eq. 8** was not effective for predicting the energies of these boundaries. It should be pointed out that although the root-mean-square error (RMSE) for arbitrary boundaries in the 5D space (0.115 J/m^2) is much greater than for the 1D (0.023 J/m^2), 2D (0.068 J/m^2), and 3D (0.065 J/m^2) subsets, it is

Table 1

Average energies and root-mean-square error (RMSE) between the simulated (ϵ_{sim}) and interpolated (ϵ_{inter}) grain boundary energies at fixed Σ.

Σ	$\theta\langle uvw\rangle$	Number of GBs	Ave. ϵ_{sim}, J/m^2	Std. Dev. ϵ_{sim}	Ave. ϵ_{inter}, J/m^2	Std. Dev. ϵ_{inter}	RMSE, J/m^2
3	60° <111>	40	0.74	0.316	0.75	0.312	0.020
5	36.87° <100>	27	1.16	0.071	1.11	0.037	0.088
7	38.21° <111>	21	1.20	0.060	1.17	0.049	0.040
9	38.94° <110>	29	1.05	0.176	1.03	0.150	0.049
11	50.48° <110>	9	0.99	0.269	0.93	0.215	0.104
13a	22.62° <100>	6	1.15	0.110	1.17	0.146	0.052
13b	27.8° <111>	9	1.17	0.044	1.14	0.017	0.045
15	48.19° <210>	19	1.22	0.064	1.22	0.033	0.065
17a	28.07° <100>	6	1.18	0.085	1.19	0.109	0.039
17b	61.93° <221>	3	0.97	0.309	0.97	0.308	0.007
19a	26.53° <110>	3	1.01	0.294	1.00	0.291	0.018
19b	46.83° <111>	5	1.24	0.161	1.12	0.102	0.133
21a	21.79° <111>	5	1.10	0.042	1.07	0.010	0.047
21b	44.42° <211>	12	1.21	0.062	1.12	0.015	0.109
23	40.46° <311>	3	1.26	0.123	1.12	0.009	0.179
25a	16.26° <100>	4	1.04	0.146	1.09	0.171	0.106
25b	51.68° <331>	8	1.17	0.076	1.05	0.015	0.133
27a	31.59° <110>	7	1.04	0.191	1.02	0.194	0.024
27b	35.43° <210>	8	1.21	0.081	1.15	0.065	0.081
29a	43.6° <100>	3	1.21	0.073	1.20	0.064	0.008
31b	52.2° <211>	3	1.09	0.056	1.17	0.052	0.094
33a	20.05° <110>	5	0.96	0.226	0.95	0.208	0.028
33b	33.56° <311>	3	1.22	0.090	1.19	0.074	0.110
33c	58.99° <110>	5	0.98	0.261	0.97	0.237	0.039
35a	34° <211>	3	1.25	0.041	1.18	0.058	0.100
35b	43.2° <331>	5	1.24	0.093	1.18	0.019	0.102
All		408	1.12	0.211	1.07	0.190	0.088

comparable with an estimated 10 % error in the MD simulated energies [26]. Even if one considers the simulated and interpolated grain boundary energies at the fixed Σ (see **Table 1**), the RMSE are also approximately 10% of average simulated energies. To validate and to quantify the predictive capability of the grain boundary energy function, the interpolated energies are compared with the energies previously simulated by Tschopp et al. [27]. As shown in **Fig. 4b**, the interpolated energies are strongly correlated with the simulated energies with a correlation coefficient of 0.98. The positive deviation of the simulated energies [27] from the interpolated energies determined by fitting to the values reported by Ratanaphan et al. [21] suggests that this might result from a difference in the number of initial configurations for each boundary. Particularly, a larger number of initial configurations for each type of grain boundary, which was used in [21] (100 – 10,000 states) compared with the ones in [27] (100 – 1,000 states), could improve the search for a global minimum boundary energy. While it is not guarantee that the smallest energy among the larger number of minimized configurations corresponds to the global minimum energy, the energies reported by Ratanaphan et al. [21] are on average lower than the ones simulated by Tschopp et al. [27]. Regardless to these differences, it should be noted that the RMSE for grain boundary energies reported by Tschopp et al. (0.049 J/m^2) are also less than an estimated 10 % error in the MD simulated energies.

The energies of 39,861 grain boundaries derived from the energy function are then compared with the measured grain boundary population [14]. These data sets include tilt, twist, and mixed grain boundaries for 1,058 different misorientations. As examples, comparisons between the interpolated grain boundary energies and the measured grain boundary population for $\Sigma 3$, $\Sigma 5$, and $\Sigma 7$ misorientations [14] are shown in **Fig. 5**. The schematic diagrams, which show the orientations of the tilt, twist, and symmetric grain boundaries are produced by GBToolbox [28–30]. The interpolated energies at the $\Sigma 3$ misorientation are inversely correlated with the measured grain boundary population [14]. Specifically, the minimum energy located at the (112) symmetrical tilt boundary (the coherent twin boundary, 0.273 J/m^2) corresponds to the maxima in the measured grain boundary population (13 MRD). The measured grain boundary population at the $\Sigma 5$ and $\Sigma 7$ misorientations [14] are not inversely correlated with the energies interpolated from our grain bound-

ary energy function. The relative areas of the minima energy boundaries located in proximity to the $\Sigma 5$ (013) and $\Sigma 7$ (123) symmetrical boundaries are relatively low compared with the boundaries with higher energies. Note that for grain boundaries with the $\Sigma 5$ misorientation, they are less observed and the distribution of the relative areas of grain boundary at this misorientation is poorly measured. **Fig. 6**. shows the point-by-point comparisons between the interpolated grain boundary energies and the measured grain boundary population [14]. Overall, the energies and population are inversely correlated as indicated by the correlation coefficient, R= -0.68 (see **Fig. 6a** and **Table 2.**). While the inverse relationships are observed for the $\Sigma 3$ (R= -0.96), $\Sigma 9$ (R= -0.53), and $\Sigma 27a$ (R= -0.57), it is not the case for the rarely observed $\Sigma 27b$ (R= 0.25) as shown in **Fig. 6b**. It should be noted that the energy anisotropies, ϵ_{aniso}, calculated from the maximum energy and minimum energy at $\Sigma 3$ (1.01 J/m^2), $\Sigma 9$ (0.53 J/m^2), and $\Sigma 27a$ (0.52 J/m^2) is larger than the $\Sigma 27b$ (0.22 J/m^2). Furthermore, $\Sigma 17b$ (ϵ_{aniso}= 0.66 J/m^2, R= -0.79), $\Sigma 33a$ (ϵ_{aniso}= 0.52 J/m^2, R= -0.70), $\Sigma 33b$ (ϵ_{aniso}= 0.42 J/m^2, R= -0.79), and $\Sigma 33c$ (ϵ_{aniso}= 0.60 J/m^2, R= -0.80) boundaries having relatively high population and energy anisotropies comparable with the $\Sigma 9$ and $\Sigma 27a$ (~ 0.5 J/m^2) also show inverse relationships in **Fig. 6c**. For the $\Sigma 5$, $\Sigma 7$, and $\Sigma 15$ grain boundaries with energy anisotropies less than 0.20 J/m^2, it is clearly demonstrated that these energies and population are not inversely correlated as shown in **Fig. 6d**. **Fig. 7**. shows comparisons between the correlation coefficients and energy anisotropies for all misorientations listed in **Table 2**. As shown in **Fig. 7**, there are two distinct clusters separated by a boundary where the energy anisotropy is equal to 0.4 J/m^2, indicating that the energy anisotropies at specific misorientations influence the relationship between the grain boundary population and energies in polycrystalline α iron. The misorientations that show poor correlations to the grain boundary population have two characteristics. First, they are relatively high in energy. For example, the $\Sigma 5$, $\Sigma 7$, and $\Sigma 15$ boundaries have almost of all their energies greater than 1.1 J/m^2 while the boundaries in **Fig. 6b** and **Fig. 6c** have most of their energies less than this value. Because of their high energies, the $\Sigma 5$, $\Sigma 7$, and $\Sigma 15$ boundaries also have low populations. Previous work has shown that the inverse correlation between grain boundary energies and populations disappears for high energy boundaries because of the
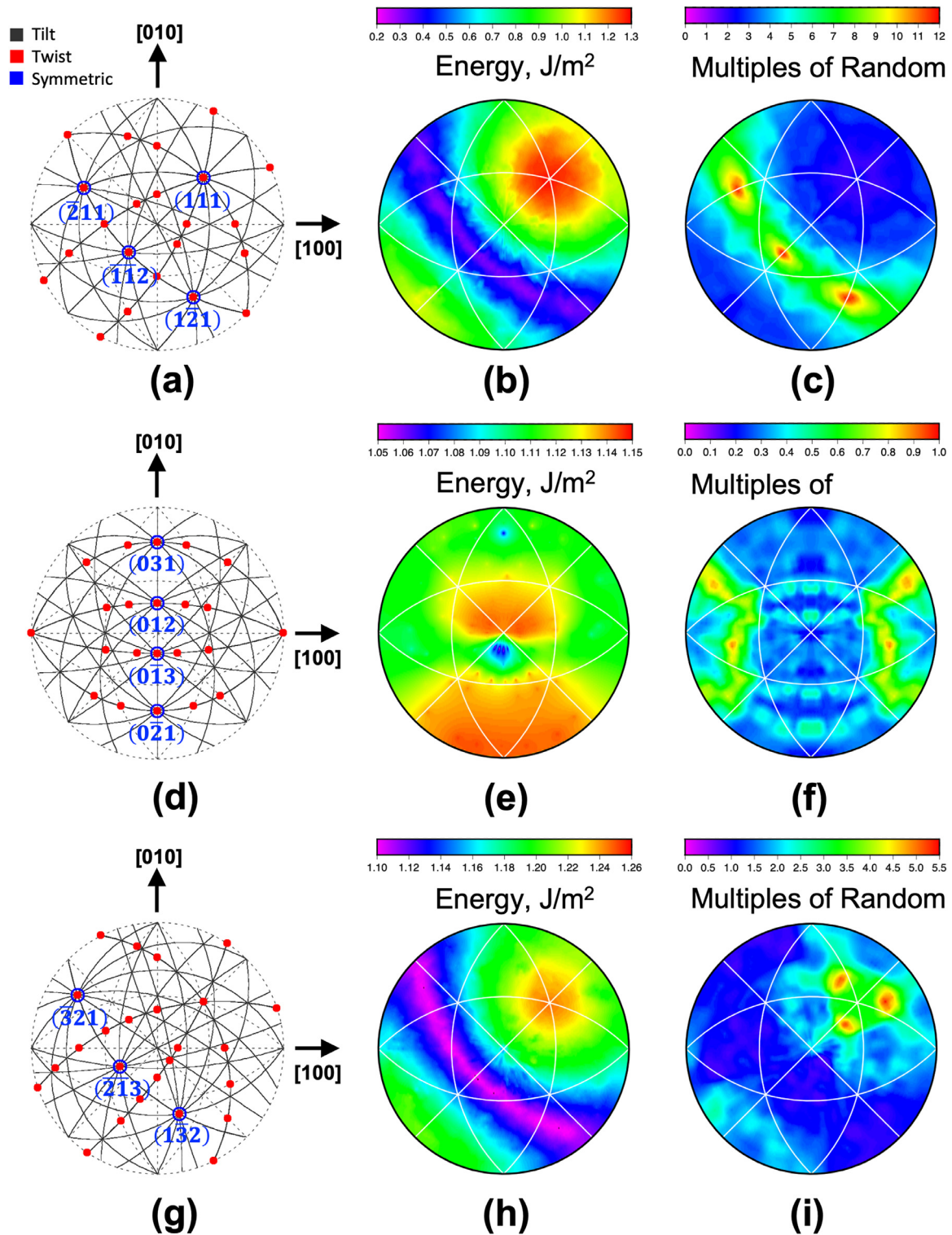
Fig. 5. Characteristic grain boundaries, shown on a stereographic projection, at Σ3, 60°/ [111] (a) Σ5, 36.86°/ [100] (d) Σ7, 38.21°/ [111] (g) generated in GBToolbox [28–30]. The distributions of grain boundary energies derived from our grain boundary energy function are compared with the measured grain boundary population for Σ3 (b, c) Σ5 (e, f) and Σ7 (h, i) misorientations [14]. The relative populations are plotted in units of multiples of a random distribution (MRD).

difficulty of accurately measuring the populations of infrequently oc-curring boundaries [31,32]. The second thing they have in common is a small energy anisotropy. In other words, during microstructure evolu-tion, the energy landscape for boundary plane orientations is relatively flat, so the energy penalty for deviating from the lowest energy orien-tation is relatively small. Considering both of these factors, it is not too

surprising that the populations of boundaries at misorientations with low anisotropy and high average energies do not correlate well with an energy function based on simulated energies. Although the energies pre-dicted by the function are less certain at high energies, these boundaries are of little interest to grain boundary engineering. For grain bound-ary engineering, we are more interested in low energy boundaries that
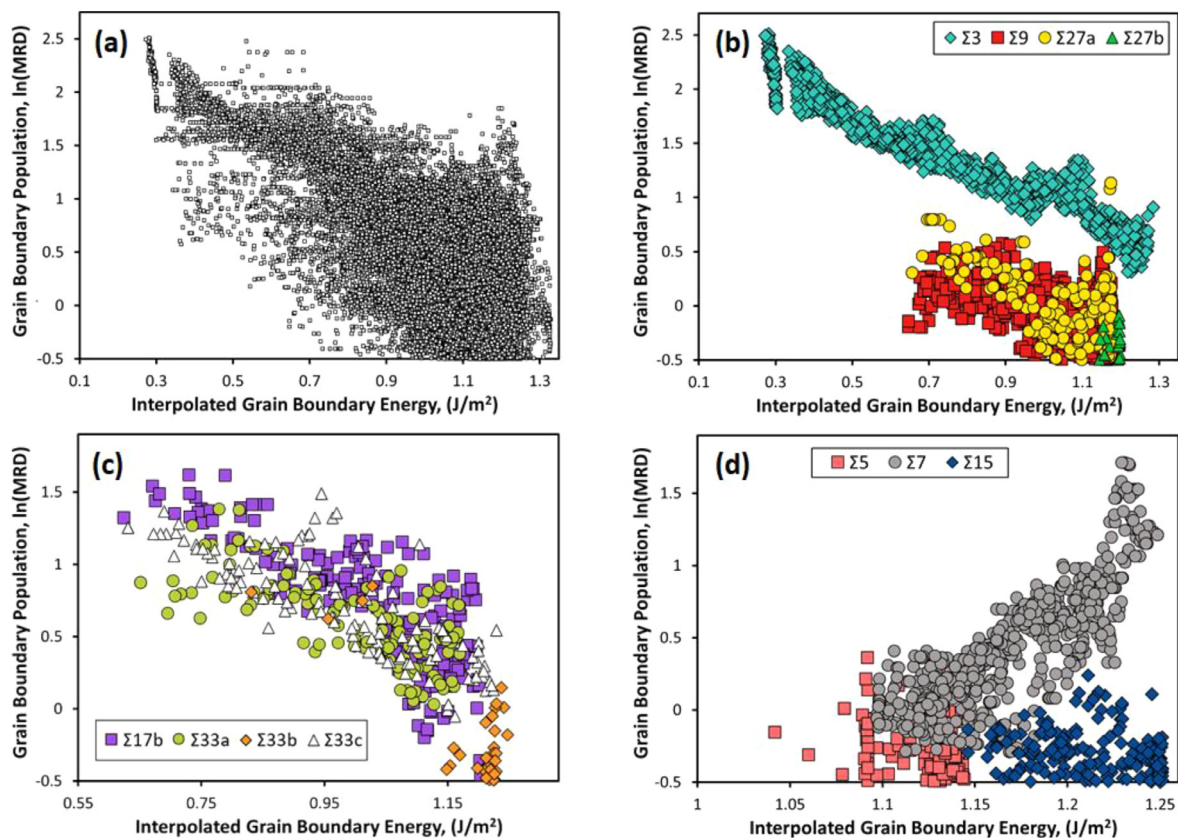
Fig. 6. Relationships between the interpolated energies and the measured grain boundary population [14] for all boundaries with logarithms of the populations of grain boundaries, ln (MRD) > - 0.5 (a), twinning-related grain boundaries, Σ3, Σ9, Σ27a, and Σ27b (b), grain boundaries with high-energy anisotropies, Σ17b, Σ33a, Σ33b, and Σ33c (c), and grain boundaries with low-energy anisotropies, Σ5, Σ7, and Σ15 (d). For interpretation of the references to color in this figure legend, the reader is referred to the web version of this article.

Table 2

Energy anisotropies (ϵ_{aniso}) are calculated from the maximum energy (ϵ_{max}) and minimum energy (ϵ_{min}). The correlation coefficients between the interpolated (ϵ_{inter}) grain boundary energies and the measured grain boundary population [14] are correlated with the energy anisotropies at fixed Σ.

| Σ	Number of GBs	ϵ_{max}, J/m^2	ϵ_{min}, J/m^2	ϵ_{aniso}, J/m^2	Correlation coefficient
3	1,436	1.285	0.273	1.012	-0.96
5	940	1.147	0.991	0.156	-0.20
7	616	1.249	1.097	0.152	0.82
9	995	1.179	0.647	0.531	-0.53
11	446	1.108	0.567	0.541	-0.58
13a	186	1.326	1.023	0.303	-0.13
13b	219	1.165	1.111	0.054	0.76
15	878	1.263	1.146	0.117	-0.23
17a	112	1.311	1.073	0.237	0.00
17b	203	1.280	0.624	0.656	-0.79
19a	171	1.179	0.660	0.520	-0.68
19b	110	1.276	0.953	0.323	-0.16
21a	169	1.074	1.050	0.024	0.68
21b	486	1.165	1.064	0.101	-0.09
23	223	1.138	0.991	0.147	0.05
25a	125	1.244	0.904	0.340	0.27
25b	417	1.073	0.997	0.076	-0.05
27a	204	1.174	0.657	0.517	-0.57
27b	362	1.216	0.994	0.222	0.25
29a	31	1.277	1.161	0.116	0.64
29b	129	1.274	1.044	0.230	0.18
31a	33	0.997	0.979	0.019	0.25
31b	104	1.210	1.108	0.102	0.11
33a	131	1.170	0.651	0.519	-0.70
33b	173	1.248	0.831	0.417	-0.79
33c	128	1.229	0.631	0.598	-0.80
35a	260	1.251	1.116	0.134	0.52
35b	222	1.225	1.091	0.134	0.21
All	39,861	1.328	0.273	1.055	-0.68
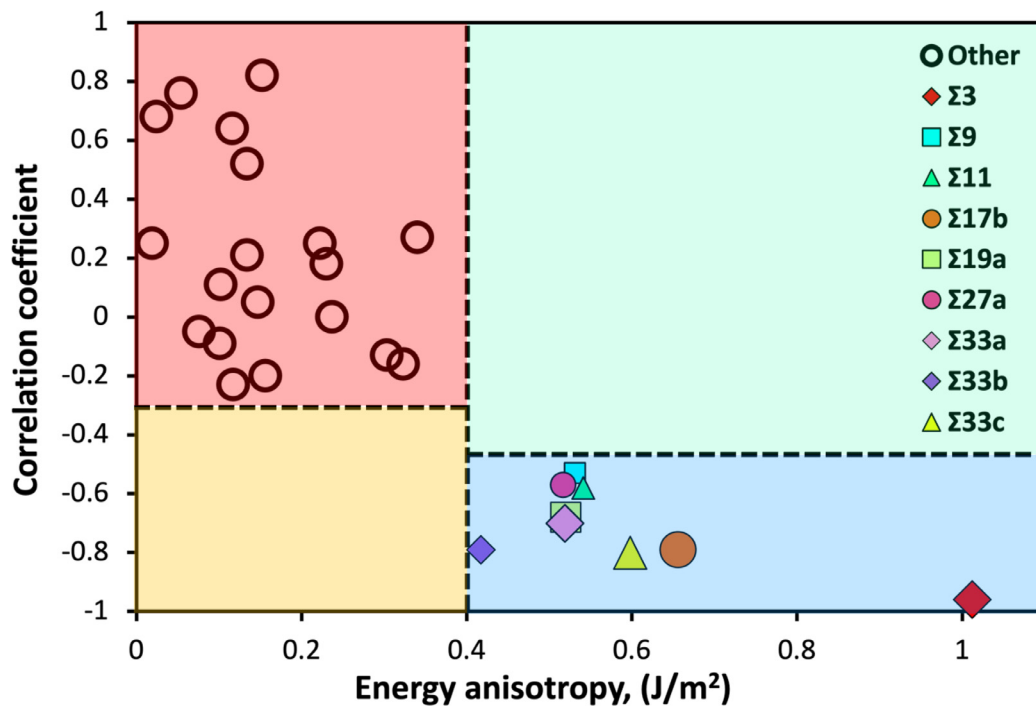
Fig. 7. Relationships between correlation coefficient and energy anisotropy for two distinct clustered groups. For the misorientations having energy anisotropies lower than 0.4 J/m², the correlation coefficients are weakly associated or positively correlated with the energy anisotropies. For $\Sigma 3$, $\Sigma 9$, $\Sigma 11$, $\Sigma 17b$, $\Sigma 19a$, $\Sigma 27a$, $\Sigma 33a$, $\Sigma 33b$, and $\Sigma 33c$ misorientations with energy anisotropies larger than 0.4 J/m², their correlation coefficients are all negative.

have significant grain boundary energy anisotropy and these are well predicted by the function. While for fcc materials grain boundary engineering focuses on the twinning-related grain boundaries ($\Sigma 3^n$), for bcc materials the most promising route is to focus on those boundaries that have both low energies and high energy anisotropy that strongly influences the GBCD.

4. Conclusion

A grain boundary energy function for α iron has been formulated from the hierarchical interpolation of scaffolding grain boundary subsets with <100>, <110>, and <111> rotation axes using Read-Shockley-Wolf (RSW) and parabolic functions. Comparisons between approximately 40,000 grain boundary energies interpolated from the new function and measured grain boundary populations reveal that energy anisotropy at a specific misorientation has the most significant influence to the grain boundary character distribution of α iron. The energy function for α iron provides a useful resource for the simulation of microstructure evolution or to foster the development of grain boundary engineering (GBE) in the α iron.

Declaration of Competing Interest

The authors declare that they have no known competing financial interests or personal relationships that could have appeared to influence the work reported in this paper.

Supplementary materials

Supplementary material associated with this article can be found, in the online version, at doi:10.1016/j.mtla.2021.101186.

References

[1] A.P. Sutton, R.W. Balluffi, Interfaces in Crystalline Materials, Oxf, Univ. Press Oxf, 1995.
[2] T. Watanabe, Grain boundary engineering: historical perspective and future prospects, J. Mater. Sci. 46 (2011) 4095–4115, doi:10.1007/s10853-011-5393-z.
[3] G. Palumbo, E.M. Lehockey, P. Lin, Applications for grain boundary engineered materials, JOM 50 (1998) 40–43, doi:10.1007/s11837-998-0248-z.
[4] G.S. Rohrer, Grain boundary energy anisotropy: a review, J. Mater. Sci. 46 (2011) 5881–5895, doi:10.1007/s10853-011-5677-3.
[5] G.S. Rohrer, Measuring and Interpreting the Structure of Grain-Boundary Networks, J. Am. Ceram. Soc. 94 (2011) 633–646, doi:10.1111/j.1551-2916.2011.04384.x.
[6] Y. Zhao, I.C. Cheng, M.E. Kassner, A.M. Hodge, The effect of nanotwins on the corrosion behavior of copper, Acta Mater 67 (2014) 181–188, doi:10.1016/j.actamat.2013.12.030.
[7] L. Lu, Y. Shen, X. Chen, L. Qian, K. Lu, Ultrahigh Strength and High Electrical Conductivity in Copper, Science 304 (2004) 422–426, doi:10.1126/science.1092905.
[8] V.Y. Gertsman, S.M. Bruemmer, Study of grain boundary character along intergranular stress corrosion crack paths in austenitic alloys, Acta Mater 49 (2001) 1589–1598, doi:10.1016/S1359-6454(01)00064-7.
[9] Y.H. Wen, H.B. Peng, D. Raabe, I. Gutierrez-Urrutia, J. Chen, Y.Y. Du, Large recovery strain in Fe-Mn-Si-based shape memory steels obtained by engineering annealing twin boundaries, Nat. Commun. 5 (2014) 4964, doi:10.1038/ncomms5964.
[10] T. Watanabe, An approach to grain boundary design of strong and ductile polycrystals, Res Mech 11 (1984) 47–84.
[11] S.Q. Cao, J.X. Zhang, J.S. Wu, J.G. Chen, Effects of GBCD on cold work embrittlement of high strength interstitial free steels, Mater. Des. 27 (2006) 53–57, doi:10.1016/j.matdes.2004.09.014.
[12] H. Beladi, G.S. Rohrer, The Distribution of Grain Boundary Planes in Interstitial Free Steel, Metall. Mater. Trans. A. 44 (2013) 115–124, doi:10.1007/s11661-012-1393-0.
[13] H. Yan, H. Bi, X. Li, Z. Xu, Effect of two-step cold rolling and annealing on texture, grain boundary character distribution and r-value of Nb+Ti stabilized ferritic stainless steel, Mater. Charact. 60 (2009) 65–68, doi:10.1016/j.matchar.2008.05.006.
[14] H. Beladi, G.S. Rohrer, The relative grain boundary area and energy distributions in a ferritic steel determined from three-dimensional electron backscatter diffraction maps, Acta Mater 61 (2013) 1404–1412, doi:10.1016/j.actamat.2012.11.017.

[15] W. Wang, S. Chen, G.S. Rohrer, W. Chen, The inter-connections of Σ3 boundaries in pure iron, Scr. Mater. 128 (2017) 18–22, doi:10.1016/j.scriptamat.2016.09.038.

[16] J. Yang, L. Fan, L. Jia, J. Wu, X. Song, L. Jiang, Microtexture Evolution and Grain Boundary Character Distribution of Interstitial-Free Steels With Moderate Levels of Cold Rolling Reductions, J. Iron Steel Res. Int. 20 (2013) 47–52, doi:10.1016/S1006-706X(13)60215-0.

[17] V.V. Bulatov, B.W. Reed, M. Kumar, Grain boundary energy function for fcc metals, Acta Mater 65 (2014) 161–175, doi:10.1016/j.actamat.2013.10.057.

[18] E.A. Holm, D.L. Olmsted, S.M. Foiles, Comparing grain boundary energies in face-centered cubic metals: Al, Au, Cu and Ni, Scr. Mater. 63 (2010) 905–908, doi:10.1016/j.scriptamat.2010.06.040.

[19] S. Ratanaphan, R. Sarochawikasit, D.L. Olmsted, G.S. Rohrer, K.N. Tu, Grain boundary character distribution in electroplated nanotwinned copper, J. Mater. Sci. 52 (2017) 4070–4085, doi:10.1007/s10853-016-0670-5.

[20] S. Ratanaphan, R. Sarochawikasit, N. Kumanuvong, S. Hayakawa, H. Beladi, G.S. Rohrer, T. Okita, Atomistic simulations of grain boundary energies in austenitic steel, J. Mater. Sci. 54 (2019) 5570–5583, doi:10.1007/s10853-018-03297-4.

[21] S. Ratanaphan, D.L. Olmsted, V.V. Bulatov, E.A. Holm, A.D. Rollett, G.S. Rohrer, Grain boundary energies in body-centered cubic metals, Acta Mater 88 (2015) 346–354, doi:10.1016/j.actamat.2015.01.069.

[22] D.M. Saylor, G.S. Rohrer, Evaluating Anisotropic Surface Energies Using the Capillarity Vector Reconstruction Method, Interface Sci 9 (2001) 35–42, doi:10.1023/A:1011262628243.

[23] H. Dette, J. Gösmann, C. Greiff, R. Janisch, Efficient sampling in materials simulation - Exploring the parameter space of grain boundaries, Acta Mater 125 (2017) 145–155, doi:10.1016/j.actamat.2016.11.044.

[24] J.K. Mackenzie, A.J.W. Moore, J.F. Nicholas, Bonds broken at atomically flat crystal surfaces—I: Face-centred and body-centred cubic crystals, J. Phys. Chem. Solids. 23 (1962) 185–196, doi:10.1016/0022-3697(62)90001-X.

[25] D. Wolf, A read-shockley model for high-angle grain boundaries, Scr. Metall. 23 (1989) 1713–1718, doi:10.1016/0036-9748(89)90348-7.

[26] T. Frolov, W. Setyawan, R.J. Kurtz, J. Marian, A.R. Oganov, R.E. Rudd, Q. Zhu, Grain boundary phases in bcc metals, Nanoscale 10 (2018) 8253–8268, doi:10.1039/C8NR00271A.

[27] M.A. Tschopp, K.N. Solanki, F. Gao, X. Sun, M.A. Khaleel, M.F. Horstemeyer, Probing grain boundary sink strength at the nanoscale: Energetics and length scales of vacancy and interstitial absorption by grain boundaries in α-Fe, Phys. Rev. B. 85 (2012) 064108, doi:10.1103/PhysRevB.85.064108.

[28] A. Morawiec, K. Glowinski, On "macroscopic" characterization of mixed grain boundaries, Acta Mater 61 (2013) 5756–5767, doi:10.1016/j.actamat.2013.06.019.

[29] K. Glowinski, On identification of symmetric and improperly quasi-symmetric grain boundaries, J. Appl. Crystallogr. 47 (2014) 726–731, doi:10.1107/S160057671400435X.

[30] K. Głowiński, GBToolbox (2021). accessed February 18, 2021. https://github.com/kglowins/gbtoolbox-legacy.

[31] G.S. Rohrer, E.A. Holm, A.D. Rollett, S.M. Foiles, J. Li, D.L. Olmsted, Comparing calculated and measured grain boundary energies in nickel, Acta Mater 58 (2010) 5063–5069, doi:10.1016/j.actamat.2010.05.042.

[32] E.A. Holm, G.S. Rohrer, S.M. Foiles, A.D. Rollett, H.M. Miller, D.L. Olmsted, Validating computed grain boundary energies in fcc metals using the grain boundary character distribution, Acta Mater 59 (2011) 5250–5256, doi:10.1016/j.actamat.2011.05.001.